ENCLOSURE 2

MFN 15-059

Responses to NRC RAIs for NEDC-33353P Submittal

Non-Proprietary Information - Class I (Public)

NON-PROPRIETARY NOTICE

This is a non-proprietary version of Enclosure 1 of MFN 15-059 which has the proprietary information removed. Portions of the document that have been removed are indicated by an open and closed bracket as shown here [[ ]].

RAI 1

Please provide additional data that has been collected since publication of the submitted licensing topical report (LTR) such as from Plants V and F or additional post irradiation examinations (PIE) from Plants G and K. Please also provide any additional channel data from Plants P and N.

RESPONSE TO RAI 1

In the –A version of the subject LTR, the review scope will be revised to exclude the application of GNF-Ziron to fuel bundle channels. See the response to RAI 2 for the pages in the LTR that are affected by this change. There remains discussion of channels in the LTR from a material standpoint, which are applicable to the review of GNF-Ziron.

This response will therefore focus on the non-channel fuel assembly components. Since the LTR submittal, inspection activities related to GNF-Ziron LUA programs have occurred at two plants in the United States (US) and at two European plants. At Plants H and V, inspections were conducted after two cycles of operation. In Europe, inspections at Plant F after 2.5 annual cycles (the half cycle was due to mid-cycle removal due to debris failure of a Zircaloy-2 rod in the assembly), and after eight annual cycles at Plant G have been completed. (The irradiation program at Plant K is complete and there is no new inspection data.)

At Plant H, the lead use program consisted of two GE14 fuel assemblies of the same configuration, each with 29 GNF-Ziron clad fuel rods and one GNF-Ziron water rod. Irradiation started in June 2009, and both lead use assemblies were removed from core after [[ ]] for off-outage inspection in early 2013, and were reinserted in 2014 for one more cycle. Inspection scope was comprised of [[ ]] from one assembly (JYG454), [[ ]] symmetric pair locations. The fuel rods were subjected to individual rod full-length 360 degree visual inspections and full-length measurements of corrosion / tenacious crud thickness using an eddy-current liftoff technique, rod diameter using profilometry, and length using a calibrated tape. The water rod was visually inspected and length measured. For visual examination, fuel rods were typically brushed first to remove non-tenacious crud. Figure 1-1 shows the configuration of different cladding types in the lead use assemblies and location of inspected rods (in red). Figure 1-2 shows views near the top of the assembly with cladding type indicated below the picture. No abnormalities were noted near the upper tie plate (left in Figure 1-2). The fuel rods show fuel length variation (right in Figure 1-2) that is typically observed for assemblies with Zircaloy-2 cladding. Note that the two Zircaloy-2 tie rods (T) show the normal, slightly longer rod lengths compared with adjacent rods; see response to RAI 13 for additional discussion on growth of tie rods compared with non-tie rods. The peripheral inspection did not reveal any unexpected behavior of GNF-Ziron fuel rods. Figure 1-3 shows the results of eddy-current liftoff measurements. The liftoff technique takes data along the axial length of the fuel rod and measures the combined thickness of corrosion oxide and crud layers present between the metallic cladding and the eddy-current probe. As the crystalline nature (structure and composition) of the deposited crud depends on the coolant chemistry, liftoff data for most boiling water reactor (BWR) fuel rods requires a correction to take into account the ferrimagnetic nature of the crud, the thickness of which in some cases can be significant over certain axial elevations. GNF typically assesses the liftoff data using a MELO (Maximum Effective LiftOff) metric, which is the maximum value [[ ]] of the corrected liftoff data. The MELO value therefore represents the [[ ]] for each fuel rod. In Figure 1-3, the MELO values for GNF-Ziron and Zircaloy-2 fuel rods are not very different from one another, and [[ ]] of GNF's fuel experience reference. Figures 1-4 to 1-6 show inspection summaries for three pairs of symmetric fuel rods. Figure 1-4 is for the C7 and G3 high enrichment interior rods. Figure 1-5 is for A5 and E1, relatively higher powered edge rods. Figure 1-6 is for H9 and J8 UO_2/Gd_2O_3 interior rods. Figure 1-7 shows the comparison between non-symmetric, but similar, higher power edge rods, F1 and K3, that operated with similar power. In each of these figures, images of each fuel rod at three axial elevations (number on lower left of each picture) are shown, together with one profilometry scan and one liftoff trace. For the liftoff trace, two traces are shown; one (red) is for liftoff without correction for ferrimagnetic nature of the crud, and one for after correction (green). GNF-Ziron and Zircaloy-2 fuel rods essentially behaved similarly and there is no indication of any abnormality for GNF-Ziron. Figure 1-8 shows visual inspection results for the GNF-Ziron water rod. The water rod was inspected without brushing to remove non-tenacious crud (due to issues with the brush for the water rod). The corrosion condition was only observable at locations where the non-tenacious crud was taken off, for example, near spacer locations due to necessary rotation during the water rod removal process; the observable corrosion is [[ ]]. The water rod length measurement [[ ]] is shown in Figure 1-9 and [[ ]]. The length measurements of four fuel rods (two GNF-Ziron and two Zircaloy-2) are shown in Figure 1-10 together with other Zircaloy-2 data. At this exposure [[ ]], the measured fuel rods lengths [[ ]] GNF-Ziron and Zircaloy-2. In Figure 1-2, the top of two measured fuel rods can be seen. The GNF-Ziron fuel rod (Z) [[ ]] the adjacent Zircaloy-2 rod (2), as can be seen in Figure 1-2.

At Plant V, the lead use program [[ ]] GNF2 fuel assemblies of the same configuration, each with 24 GNF-Ziron cladding fuel rods. Irradiation started in 2007 and finished at the end of 2014 when the plant shut down. Inspections were conducted after one and two cycles of operation. Results from the first inspection were included in the LTR and additional information is provided in response to RAI 4. Results from the second inspection [[ ]] are discussed below. The location of the lead use assembly (LUA) in the two cycles is shown in Figure 1-11. The figure also shows the location of the inspected rods (red circles) with the GNF-Ziron rods indicated in yellow. The location of the inspected LUA in the second cycle was near the core edge, where the fast neutron flux gradient is high. The inspected rods included a pair of symmetrically positioned GNF-Ziron and Zircaloy-2 rods. As a consequence of the assembly being located in a location with high flux gradient, the pair of rods did not experience the same operational condition during the second cycle. The inspection scope included bundle periphery visual examination and fuel rod visual and measurements of corrosion crud using an eddy-current liftoff technique and rod diameter using profilometry. Peripheral pictures near the upper tie plate are shown in Figure 1-12. The peripheral visual inspection did not reveal any unexpected behavior of GNF-Ziron fuel rods. Figures 1-13 to 1-16 show inspection summaries for the four inspected GNF-Ziron Fuel rods, together with symmetric or similar Zircaloy-2 fuel rods. In each of these figures, images of each fuel rod at three axial elevations are shown, together with one profilometry scan and one liftoff trace. Figure 1-13 shows the results of the A8 / H1 symmetric pair of edge rods. As noted above, the near-core periphery location of the assembly during the second cycle of operation (prior to inspection) meant that the two rods experienced different operation conditions, with the H1 Zircaloy-2 rod positioned closer to the extreme edge of the core than the A8 GNF-Ziron rod (see Figure 1-11). Results in Figure 1-13 show that the A8 rod (GNF-Ziron) exhibited [[ ]] compared with the H1 (Zircaloy-2) rod, and the differences in MELO value can be attributed to [[ ]] in the second cycle. Figure 1-14 shows results for the K10 [[ ]] and A1 [[ ]]. Figure 1-15 shows results for the H10 [[ ]] and K8 [[ ]]. Figure 1-16 shows results for the H9 [[ ]]. It is noted that Zircaloy-2 rods at spacer locations (~18, 36 and 55 inch elevations) often exhibited more nodules, an indication of shadow corrosion, a condition also noted after the first cycle of operation.

At Plant G, the LUA program consisted of GE14 fuel assemblies with all GNF-Ziron fuel cladding. Inspection was conducted at [[ ]] exposure after eight annual cycles of operation. The inspection scope included visual examination of bundle periphery, and visual examination and measurements of corrosion and crud using an eddy-current liftoff technique and diameter using profilometry on one GNF-Ziron fuel rod. Length measurements were also taken for a water rod and the bundle. Figure 1-17 shows normal visual appearance near upper tie plate of the fuel assembly. Figure 1-18 shows one profilometry scan and one liftoff trace for the inspected GNF-Ziron rod together with visual appearance (after brushing) of the rod at several elevations. The liftoff and profilometry results reflect [[ ]]. The water rod length results are shown in Figure 1-9. Bundle growth data for GNF-Ziron assemblies obtained from the LUA program at Plant G is compared with data for other Zircaloy-2 10x10 fuel assemblies in Figure 1-19.

At Plant F, the GNF2 fuel assembles were inspected [[ ]] in 2010 and 2013. The 2010 inspection was limited to a peripheral visual examination. The appearance near the upper tie plate is shown in Figure 1-20. The visual examination did not reveal any unexpected features such as variances in fuel rod length. In the 2013 inspection, the fuel assembly was visually inspected; however, the upper tie plate region was blocked from the video camera. The rest of the bundle showed no unusual features. Three GNF-Ziron rods were visually inspected, as was a Zircaloy-2 rod symmetric to one of the GNF-Ziron rods.

Figure 1-21 shows the results of the A8 / H1 symmetric pair of edge rods. Figure 1-22 shows results of the other two GNF-Ziron rods. No remarkable features were noted in the inspected rods.

[[

]]

Figure 1-1 Configuration of GE14 LUA at Plant H

[[

]]

Figure 1-2 Visuals Near Upper Tie Plate from Plant H After Two Cycles

[[

]]

Figure 1-3 Summary of Liftoff Measurements from Plant H After Two Cycles

[[

]]

Figure 1-4 Summary of JYG454 C7 and G3 Rods from Plant H After Two Cycles
Top and bottom pictures for each rod are from spacer locations.

[[

]]

Figure 1-5 Summary of JYG454 A5 and E1 Rods from Plant H After Two Cycles Bottom picture for each rod is from a spacer location.

[[

]]

Figure 1-6 Summary of JYG454 H9 and J8 Rods from Plant H After Two Cycles Top and bottom pictures for each rod are from spacer locations.

[[

]]

Figure 1-7 Summary of JYG454 F1 and K3 Rods from Plant H After Two Cycles Bottom picture for each rod is from a spacer location.

[[

]]

Figure 1-8 Visuals (Unbrushed) JYG454 Water Rod from Plant H After Two Cycles

[[

]]

Figure 1-9 GNF-Ziron Water Rod Growth Data and Zircaloy-2 Data from Plants H and G

[[

]]

Figure 1-10 GNF-Ziron Fuel Rod Growth Data and Zircaloy-2 Data from Plants H and G

[[

]]

Figure 1-11 GNF-Ziron LUAs Core Locations in Plant V During C26 (top) and C27 (bottom)

[[

]]

Figure 1-12 Visuals Near Upper Tie Plate from Plant V After Two Cycles

[[

]]

Figure 1-13 Summary of JYA804 A8 and H1 Rods from Plant V After Two Cycles
Top and bottom pictures for each rod are from spacer locations.

[[

]]

Figure 1-14 Summary of JYA804 K10 and A1 Rods from Plant V After Two Cycles
Middle and bottom pictures for each rod are from spacer locations.

[[

]]

Figure 1-15 Summary of JYA804 H10 and K8 Rods from Plant V After Two Cycles
Top and bottom pictures for each rod are from spacer locations.

[[

]]

Figure 1-16 Summary of JYA804 H9 Rod from Plant V After Two Cycles

[[

]]

Figure 1-17 Visuals Near Upper Tie Plate from Plant G After Eight Annual Cycles

[[

]]

Figure 1-18 Summary of KG32568 G6 Rod from Plant G After Eight Annual Cycles

[[

]]

Figure 1-19 GNF-Ziron Bundle Growth Data from Plant G Compared with Zircaloy-2 Database

[[

]]

Figure 1-20 Visuals Near Upper Tie Plate from Plant F after 2.5 Cycles

[[

]]

Figure 1-21 Visuals of GNR600 A8 and H1 Rods from Plant F After 2.5 Cycles

[[

]]

Figure 1-22 Visuals of GNR600 K1 and K8 Rods from Plant F After 2.5 Cycles

RAI 2

Please compare the GNF-Ziron channel bow data to current Zircaloy-2 (Zr-2) channel bow data noting differences and analysis of why the differences exist. What are the assumed uncertainties applied to the analysis of GNF-Ziron channel bow. How do these compare to those used for current generation Zr-2 [[ ]]. Please provide an analytical example of how channel bow due to growth is subtracted from the bow measurement data to determine bow due to shadow corrosion (hydriding). This should include justification for the GNF-Ziron channel growth correlation. Have hydrogen measurements been performed on channel faces to confirm differences in hydrogen and the influence on bow?

RESPONSE TO RAI 2

This RAI is related to the application of GNF-Ziron for application as channel material. Since the submission of this LTR, GNF has submitted a separate LTR for the use of NSF, a Nb-Sn-Fe containing Zr-alloy for use as channel material. Accordingly, the application of GNF-Ziron for channel use will be removed from the GNF-Ziron LTR.

In the –A version of the subject LTR, the review scope will be revised to exclude the application of GNF-Ziron to fuel bundle channels. The three pages in the LTR that are affected by this change are included in the RAI 2 response. There remains discussion of channels in the LTR from a material standpoint, which are applicable to the review of GNF-Ziron.

EXECUTIVE SUMMARY

This document provides the technical justification to apply GNF-Ziron, a zirconium alloy with composition modified from that of Zircaloy-2, which Global Nuclear Fuel - Americas, LLC (GNF) currently utilizes in GNF fuel designs for fuel rods, spacers and water rods. GNF has performed testing and analyses to determine that GNF-Ziron is equivalent, or superior, to Zircaloy-2 with respect to physical requirements, thermal-mechanical performance criteria, as well as other operational performance criteria such as corrosion resistance and hydrogen absorption for application within specified GNF fuel assembly components. However, at this time, GNF is not requesting United States Nuclear Regulatory Commission (NRC) approval for the use of GNF-Ziron as a channel material.

3.0 Methods and Licensing Assessment

This section reviews the criteria for demonstrating compliance to GNF fuel design licensing criteria, including compliance to NRC approved methodologies. For convenience, the licensing assessment is divided in three major groups: compliance to fuel design licensing criteria; compliance for the nuclear-thermal-hydraulic analyses that are performed with the GNF core simulator; and compliance for the thermal-mechanical analyses that are more closely linked to the material performance of a new alloy such as GNF-Ziron.

3.1 Fuel Design Licensing

GNF licenses fuel designs with the NRC based on specific analyses performed in accordance with the fuel licensing acceptance criteria as specified in GESTAR II (Reference 1.1). The fuel licensing acceptance criteria included in GESTAR II establishes the basis for evaluating new fuel designs, developing the critical power correlation for these designs, and determining the applicability of generic analyses to these new designs. Compliance with the fuel licensing acceptance criteria constitutes NRC acceptance of the fuel design without specific NRC review.

The GESTAR II licensing criteria are applicable to fuel design licensing but not necessarily adequate to determine the licensing requirements of a component material. The application of GNF-Ziron as a component material within a specific fuel design will require revision of the appropriate compliance report. In this regard, this document provides justification that GNF-Ziron is capable of meeting current licensing acceptance criteria per GESTAR II. Incorporation of GNF-Ziron into GNF fuel designs would occur on a component-by-component basis by providing appropriate analyses supporting an amendment to the GNF compliance reports for a specific fuel design. Where specific NRC regulations limit application of GNF-Ziron, such as 10 CFR 50.46 Appendix K, GNF will provide justification and request an exemption prior to first application of the material in a plant.

3.2 Nuclear & Thermal/Hydraulic Methods

GNF methodologies are, in general, not dependent on composition of the fuel lattice, except for the maximum enrichment of Uranium and Gadolinia in the fuel pellets. The introduction of GNF-Ziron as a material for cladding ~~and channels~~ does not require a change to the approved nuclear and thermal hydraulic methodologies. However, there are GNF-Ziron properties that are briefly addressed in this section due to their relative importance within GNF's methodologies. They are the thermal conductivity, heat capacity, neutron absorption, irradiation growth and hydrogen absorption. The first two parameters, thermal conductivity and heat capacity, are discussed in Appendix B where it is concluded that these properties are [[
]]

The third parameter, neutron absorption, will address the effect of relative changes in the composition [[ ]] between GNF-Ziron and Zircaloy 2. Using thermal neutron activation microscopic cross sections and the isotopic and compositional abundance in the alloy, an estimation of the macroscopic cross section can be obtained. The relative change in macroscopic cross section of Zirconium in GNF-Ziron is [[

4.0 Mechanical Design Assessment

In this section, the effect of applying GNF-Ziron material to GNF fuel bundle components is evaluated with respect to GNF's fuel bundle mechanical design bases. All fuel bundle components that are currently made of Zircaloy-2 (or Zircaloy-4) material may potentially be made from GNF-Ziron material. This list of components includes fuel rod cladding, water rods, fuel spacers, ~~channels~~ and end plugs, but not channels.

The effects on fuel rod thermal-mechanical licensing methodologies are discussed in Section 3.3. Additional evaluations performed as part of the fuel bundle mechanical design basis for the fuel rod as well as other Zircaloy components are shown in Table 4-1. Although not directly addressed in Section 3.3 or Table 4-1, high resistance to fretting (both with and without debris) is a key feature of GNF fuel assemblies. The resistance is achieved by including assembly design features to minimize fretting wear on the fuel rods at spacer contact points and to minimize ingress of debris in conjunction with the inherent fretting resistance of GNF cladding. The fretting resistance of the cladding depends upon the elastic properties of the material, including the hardness. As noted in Section 3.3 and Appendix B, these properties are only weakly dependent upon alloy composition but strongly dependent upon fabrication process, specifically the final heat treatment. Because [[

]]

In summary, the GNF-Ziron properties that are of primary importance in assessing the adequacy of the fuel bundle mechanical design are: elastic properties (Young's Modulus, Poisson's Ratio), thermal expansion, thinning due to corrosion, tensile strength (yield and ultimate), creep properties, fatigue and stress rupture life, crack growth rate and thresholds, irradiation growth, and hydrogen uptake. As discussed in Section 2.1, the material properties of GNF-Ziron are [[

]] There are no negative effects to the mechanical design bases for GNF fuel from changing bundle components from a Zircaloy-2 material to GNF-Ziron. Therefore, whether or not a fuel component is important to safety, it follows that all fuel components that are currently made from Zircaloy-2 may be changed to GNF-Ziron [[

]]

RAI 3

Corrosion at the inner diameter (ID) cladding is important for loss-of-coolant accident (LOCA) embrittlement criteria. Please provide measured oxide thickness of ID cladding corrosion for high burnup fuel rods.

RESPONSE TO RAI 3

GNF-Ziron inner fuel cladding surface oxide thicknesses have been measured after irradiation to a bundle average exposure of [[ ]]. The cladding examined includes both barrier and non-barrier materials. For barrier materials, the inner surface is not a GNF-Ziron material. Average oxide thickness values for different fuel rods and sampling elevations are summarized in Table 3-1, below. The average inner surface oxide thickness ranges between [[ ]]. The thickness values were determined by optical microscopy on polished cross-sections. The reported values may represent the combined thickness of the cladding inner surface oxide layer and the pellet bonding layer because the two layers have similar contrast optically and are therefore difficult to differentiate.

Table 3-1 Average Oxide Thickness Values for Different Fuel Rods and Sampling Elevations

Rod	Cladding Type	Axial Elevation (mm)	Cladding Inner Surface Average Oxide Thickness* (microns)
[[			

]]

RAI 4

The discussion of shadow corrosion on page 2-8 only discusses one set of symmetrical Zr-2 and GNF-Ziron clad rods in Plant V, however, there were several sets of symmetrical rods in the different lead use assemblies (LUAs) in Plants V, K, and G. Please provide similar details and discussion of the shadow corrosion in other rod pairs. Are there any all-Inconel spacers in US plants?

RESPONSE TO RAI 4

Data most relevant to shadow corrosion are from GNF2 fuel assemblies that have all-Inconel spacers. In the US, most plants with GNF fuel operate, or are about to load, GNF2 assemblies. [[ ]] GNF2 assemblies are in operation as of March 2015. This quantity is updated at the annual GNF technology update with the NRC. Of these, Plants V and H have GNF-Ziron LUAs. In Europe, Plant F has GNF2 LUAs with GNF-Ziron. The GNF2 LUAs with GNF-Ziron cladding at Plant V has been inspected after two cycles of operation (see response to RAI 1). At Plant F in Europe, peripheral visual inspection was conducted after two annual cycles of operation, see the response to RAI 1 for details. Inspection after ~2.5 cycles included examinations of three GNF-Ziron rods and one Zircaloy-2 rod (not symmetric to any of the GNF-Ziron rods), as shown in Figures 1-21 and 1-22 in the response to RAI 1. Most recent data from the GNF2 LUA at Plant V was after two cycles of operation, and Figures 1-13 through 1-16 in the response to RAI 1 show summaries of the inspection results with three sets of symmetric pairs. As noted in the response to RAI 1, core location of the LUAs during the second cycle meant that rods symmetrically located in the fuel assembly likely did not experience similar operation because of neutron flux variation. In Figures 1-13 through 1-16 in the response to RAI 1, shadow corrosion response, as indicated by corrosion nodules, can be observed at ~18, 36 and 56 elevations. The visual observations are consistent with observations after one cycle of operation, as discussed in Section 2.4.2 of the LTR. Note that each data point in Figure 2-17 of the LTR [[

]]
Figure 2-18 of the LTR shows some examples of shadow corrosion appearance at spacer locations. Additional comparisons of shadow corrosion response at spacer locations between symmetric rods after one cycle of operation are presented in Figures 4-1 through 4-5 for, respectively, A3/C1, C10/K3, F9/J6, C5/E3 and A10/K1 GNF-Ziron/Zircaloy-2 pairs.

New inspection data from LUAs of the GE14 design, with Inconel springs in otherwise mostly Zircaloy-2 or GNF-Ziron spacers, from Plants H and G obtained since the submittal of the LTR are summarized in the response to RAI 1. At Plant H, where GNF-Ziron LUAs are present in both GE14 and GNF2 designs, a detailed inspection was conducted after two cycles of operation of the GE14 LUA as described in more detail in the response to RAI 1. Figures 1-4 to 1-7 in the response to RAI 1 show several examples of symmetric GNF-Ziron vs. Zircaloy-2 comparisons at spacer locations (~18 and 36 inch). At Plant G, GNF-Ziron LUAs (GE14) were inspected at [[ ]] after eight annual cycles, and appearance of one GNF-Ziron cladding at spacer locations (~36 and 55 inch elevation) are shown in Figure 1-18 in the response to RAI 1; however, although planned, inspection of other GNF-Ziron rods and companion Zircaloy-2 rods were not completed.

As noted earlier, GNF2 is a design with all-Inconel spacers, and is operating in the [[ ]]. GNF recently completed inspections at a US plant on a GNF2 LUA operated for four 24-month cycles, [[ ]] average exposure. Although this bundle has Zircaloy-2 cladding (no GNF-Ziron) the end of life (EOL) shadow corrosion observations are relevant as [[ ]] shadow corrosion performance compared with Zircaloy-2. The inspected GNF2 LUA is [[ ]] GNF2 to date. The general corrosion and shadow corrosion performance [[ ]] on cladding beneath the spacers. Figure 4-6 illustrates the liftoff (MELO) values for three measurement points in the bundle lifetime. (Note that the MELO value for each rod is the [[ ]]) Figure 4-7 illustrates the cladding appearance under lower elevation spacer contact areas, where shadow corrosion is typically most evident.

[[

]]

Figure 4-1 **Figure 4-2**

[[

]]

Figure 4-3 **Figure 4-4**

[[

]]

Figure 4-5

[[

]]

Figure 4-6 GNF2 LUA (Zircaloy-2 Clad) Liftoff Through End of Life

[[

]]

Figure 4-7 Examples of the Visual Appearance of Zircaloy-2 Cladding Under All-Inconel X-750 Spacers in GNF2, [[

]]

RAI 5

What is the range of primary coolant chemistry in US plants, specifically for O, H, Zn, sulfates, and pH? What is the range of chemistry tested for GNF-Ziron cladding? Provide this for each testing program.

RESPONSE TO RAI 5

All US BWR plants follow the Electric Power Research Institute (EPRI) BWR water chemistry guidelines, for feedwater and reactor water. All US plants mitigate intergranular stress corrosion cracking (IGSCC) by maintaining a reducing (non-oxidizing) environment in the reactor coolant, through the use of hydrogen water chemistry (HWC) (small number of plants, ~5) or NobleChem™ (most of the fleet, ~30 plants). pH is neither a control, nor a diagnostic parameter, for BWRs; operation is very close to 7 (neutral) for all plants. Because additives to control pH are not used for BWR condensate and feedwater, the pH is neutral (Reference 5-1). Hydrogen and oxygen are not control parameters in BWR reactor coolant, particularly within the core area. Reactor water hydrogen data is not required to be measured or reported; however feedwater hydrogen data is typically collected as a diagnostic parameter. For HWC plants, the feedwater hydrogen is set based on modeling of oxygen levels around the reactor system with the goal of maintaining reducing conditions. For HWC plants, feedwater hydrogen concentrations range from 1 to 2 ppm. For NobleChem™ plants, feedwater hydrogen is much lower, set to simply maintain excess hydrogen conditions. For NobleChem™ plants, typical feedwater hydrogen concentrations [[ ]]. Reactor water oxygen is a diagnostic parameter, measured continuously, used mainly for assessing the effectiveness of IGSCC mitigation measures, in out-of-core areas. Oxidizing species, and hydrogen, are produced in large concentrations within the core from radiolysis. These gases become part of the steam flow and are the main constituents removed by the condenser steam jet air ejector system → offgas system → stack.

All US BWRs use Zn injection to help mitigate after shutdown dose rates; Zn injection works in several ways (Reference 5-2):

- Reducing the growth of oxide films on stainless steel surfaces, thereby reducing the number of sites available for the incorporation of cobalt-60 (Co-60)
- Zn competes with cobalt for the sites
- Zn tends to make the fuel crud deposit more tenacious, thereby retaining Co-60 on the fuel crud, rather than releasing it to the coolant after activation, for possible deposition on piping surfaces

Reactor water Zn concentrations in US BWRs range from [[ ]] Reactor water Zn concentration is controlled by both the feedwater Zn injection rate [[ ]]and by the amount of iron that is present. Reactor water Zn is not a control parameter; operating experience has shown that maintaining a certain relationship (ratio) between the reactor water Co-60 activity (µCi/ml) and reactor water Zn (ppb) is reflected in stable, or decreasing, after shutdown dose rates. Plants with low feedwater Fe inputs, and low fuel crud, can achieve reactor water Zn levels of [[ ]]. Plants with higher feedwater Fe inputs [[ ]] with similar feedwater Zn injection rates. Dozens of fuel inspections (visual and measurements) have indicated satisfactory crud and corrosion performance over this entire range of feedwater Fe and Zn concentrations, with small variability in corrosion measurements (based on the eddy current liftoff method that measures combined oxide and crud thickness) through end of life exposures.

Sulfate is an important control parameter for IGSCC mitigation. Action Level 1 during power operation for BWRs is [[ ]]. The 2008 revision of BWRVIP-190, Water Chemistry Guidelines (Reference 5-1) reports that the 2007 US BWR fleet average for reactor water sulfate (power operation) was [[ ]]. Most US BWRs meet the EPRI sulfate goal in non-transient conditions. Based on fuel inspection data available after numerous industry transients over the years (condenser leaks and inadvertent resin intrusions with large sulfate excursions) [[ ]].

The operation experience of GNF-Ziron is discussed in Section 2.2 of the LTR. Specific to cladding, the water chemistry operated in includes normal water chemistry (NWC) with high and low feedwater Fe contents, and HWC with Zn injection and with NobleChem$^{\text{TM}}$, as summarized in Table 5-1, with reactor water average sulfate, zinc, and oxygen levels typically being [[ ]], respectively.

Table 5-1 Reactor Water Chemistry Regimes for Plants with GNF-Ziron Fuel and Channels

Plant	Component	Water Chemistry "Regime"
[[		
		]]

Notes:

[1] Noble Metal Chemical Application

[2] On-Line NobleChem

References

5-1 “BWRVIP-190: BWR Vessel and Internals Project, BWR Water Chemistry Guidelines – 2008 Revision.” EPRI, Palo Alto, CA: 2008. 1016579.

5-2 Wood, Chris, EPRI, “Zinc Injection Reduces Radiation Buildup,” Reprinted from Nuclear Engineering International, April, 1991.

RAI 6

Please provide comparison of hydrogen distribution and orientation between Zr-2 and GNF-Ziron in fuel rod cladding, spacers, end plugs, and channels. Will the changes between Zr-2 and GNF-Ziron impact the stress level at which hydride reorientation will be experienced? Please provide data to verify this response?

RESPONSE TO RAI 6

Hydride distribution and orientation in Zircaloy-2 and GNF-Ziron are functions of the material hydrogen solubility limit, the fabrication history (texture and grain size), and the temperature and stress history. The solubility limit for GNF-Ziron is essentially identical to Zircaloy-2 (Reference 6-1). As discussed in Reference 6-2, [[ ]] from that of Zircaloy-2 (including texture and grain size). The response to RAI 7 additionally discusses [[ ]] Fuel assembly component temperature and stress history are application dependent parameters and GNF-Ziron components are intended for the same application as corresponding Zircaloy-2 components. As a result, for components with similar hydrogen levels, [[ ]]. However, as noted in Reference 6-2, when corrosion is accelerated, for example, at long residence times, [[ ]].

The distribution of hydrides has been confirmed by the metallography shown in Figures 6-1 through 6-4. In these figures, metallographic samples have been etched to reveal hydrides, which show up as dark plates or segments. The figures show [[ ]] between GNF-Ziron and Zircaloy-2 in open-ended cladding (Figure 6-1), in fuel cladding (Figures 6-2 and 6-3), and in the water rod (Figure 6-4). In Figure 6-1, increased corrosion has occurred, and the hydrogen content for GNF-Ziron [[ ]] Zircaloy-2, and the two alloys show [[ ]]. For the cladding and water rod examples in Figures 6-2 through 6-4, GNF-Ziron and Zircaloy-2 have [[ ]]. For other fuel assembly components made from GNF-Ziron, such as spacers and endplugs (note that GNF-Ziron will not be applied as channel material, even though the discussions here do apply from a material processing and performance perspective), [[ ]] once sufficient hydrogen has been absorbed.

Regarding hydride reorientation, existing hydride must first be dissolved, usually when there is a temperature rise; the dissolved hydrogen can then re-precipitate under stress to a different orientation during subsequent cooling. Material parameters that need to be considered are the material microstructure and texture, the hydrogen content, the terminal solubility limit for hydride dissolution and for precipitation, TSS_d and TSS_p, respectively. As GNF-Ziron will be [[

]] for the two alloys. The hydride dissolution and precipitation behaviors (i.e., TSS_d and TSS_p), respectively, for GNF-Ziron have been investigated, and as Reference 6-1 shows, Zircaloy-2 and GNF-Ziron show the same the hydride dissolution and precipitation behaviors. For the same imposed parameters (i.e., stress level and thermal conditions) and for the same level of hydrogen, GNF-Ziron and Zircaloy-2 are therefore [[

]] for GNF-Ziron and Zircaloy-2.

References

6-1 K. Une, S. Ishimoto, "Dissolution and precipitation behavior of hydrides in Zircaloy-2 and high Fe Zircaloy," Journal of Nuclear Materials, 322 (2003) 66-72.

6-2 Global Nuclear Fuel, "Application of GNF-Ziron to GNF Fuel Designs," NEDC-33353P, Revision 0, December 2010.

[[

]]

Figure 6-1 Hydride Distribution in Zircaloy-2 and Ziron

[[

]]

[[

]]

Figure 6-2 Hydride Distribution in Fuel Rod Cladding from Plant G

[[

]]

[[

]]

Figure 6-3 Hydride Distribution in Fuel Rod Cladding from Plant G

[[

]]

[[

]]

Figure 6-4 Hydride Distribution in Zircaloy-2 and Ziron

[[

]]

RAI 7

The discussion in the LTR regarding GNF-Ziron in-reactor behavior demonstrates that cladding texture and second phase particles (SPPs) are both important components of behavior. The subject LTR includes a brief discussion on texture and SPPs for GNF Ziron stating [[

]].

a. What are the texture and SPP size distributions for the different LUA's cladding, spacer grids, water rods, and channels with GNF-Ziron?

b. What fabrication specifications will be applied to texture and SPPs for GNF-Ziron in production and how do these compare to current generation Zr-2 specifications for each of the assembly components?

c. Are there different compositions or texture or SPP specification differences between the various assembly components and if so, how does this impact material performance?

RESPONSE TO RAI 7

It is instructive to address Part b first.

b. *What fabrication specifications will be applied to texture and SPPs for GNF-Ziron in production and how do these compare to current generation Zr-2 specifications for each of the assembly components?*

[[

]].

a. *What are the texture and SPP size distributions for the various LUA's cladding, spacer grids, water rods and channels with GNF-Ziron?*

Texture: For polycrystalline metals, such as hexagonal close-packed Zr and its alloys that deform in an anisotropic manner, processing steps such as extrusion, pilgering or rolling results in preferential alignment of the grains. Annealing heat treatments, in particular those that result in grain recrystallization, will modify the alignment of the grains, resulting in a crystallographically textured (i.e., non-random, polycrystalline) material. For a manufacturing sequence that involved multiple stages of deformation followed by annealing, the degree of final deformation and condition used for the subsequent final anneal have a dominant effect on the final texture. Consistent texture is obtained when the process parameters are unchanged for materials that undergo similar deformation and recrystallization behavior. The LTR showed that [[

]], as discussed in Section A.3.a of the LTR. In order to ensure consistent texture, the deformation sequence and the recrystallization conditions are controlled under GNF's quality assurance and change management programs, rather than through controls on texture. [[

]] In the context of ensuring consistency in resultant texture, the relevant controlled process parameters are the [[
]].

As stated above, [[
]] for production and for use in LUAs. As an example, for 10x10 cladding [[

]]. The resultant texture, in terms of the Kearns factor for the basal plane, in GNF-Ziron and Zircaloy-2 is shown in Figure A-2 of the LTR and is also shown in Table 7-1 below, obtained during the manufacture of cladding used in LUA programs. The data presented is [[
]]. The LTR gives a second example in Figure A-2 for channel strips, [[
]]. The manufacture sequence for channel strip involves a sequence of hot and cold rolling to final size with intermediate and final anneals; the exact reduction amount can vary depending on the final strip thickness. For the channel strip data shown Figure A-2, both GNF-Ziron and Zircaloy-2 channels strips were [[

]]
as shown below.

Table 7-1 Texture in Terms of Kearns Factor for GNF-Ziron and Zircaloy-2

Cladding	**[[**		
Zircaloy-2			
GNF-Ziron			]]

Spacer Strip	**[[**		
Zircaloy-2			
GNF-Ziron			]]

Water Rod	**[[**		
Zircaloy-2			
GNF-Ziron			]]

SPP size distribution: As stated in Section A.3.c of the LTR, SPPs are formed when GNF-Ziron or Zircaloy-2 is processed or thermally exposed at temperatures below the solvus temperature for the SPP. Key process steps that affect the nucleation and growth of the SPPs include the cooling or quench rate following the beta-anneal step of the process. During the hold period in the beta-phase, all alloying elements associated with SPPs are taken back into solid solution. During cooling from the beta phase, SPPs are nucleated and some initial growth can occur. The SPPs grow during subsequent thermal exposure at lower temperatures, including during recrystallization anneals. The size distribution of SPPs are thus governed by the cooling rate from beta-anneal and subsequent thermal anneal, both are controlled directly by GNF or through sub-suppliers. Measurements of this attribute tend to be difficult as transmission electron microscopy is required. GNF historically has measured this attribute on Zircaloy-2 components produced to current processes. GNF-Ziron has been measured, [[
]].

The SPP size near the cladding outer surface of GNF-Ziron and Zircaloy-2 [[
]]
are shown in Section A.3.c (Tables A-2 and A-3) of the LTR. The distribution of SPPs in a given material is generally described by the average or median parameters obtained from measurements made on typically more than 200 SPPs in the material. Example distributions of SPPs in GNF-Ziron and Zircaloy-2 cladding [[ ]] are shown below in Table 7-2. These results show that the size distribution of SPPS in GNF-Ziron and Zircaloy-2 [[
]]. A typical distribution of SPPs in a water rod is shown below. The average SPP size for water rods is [[
]] discussed in Section A.3.c of the LTR. For spacer strip, [[
]] and typical distribution of SPPs is shown below.

Table 7-2 Example Distributions of SPPs in GNF-Ziron and Zircaloy-2 Cladding

[[	
	]]

c. *Are there composition, texture, or SPP specification differences between the various assembly components, and if so, how do these differences impact material performance?*

Composition specifications for the various GNF-Ziron components [[ ]]. As discussed in Parts a and b, texture and SPP size can differ between the various components because of differences in fabrication processes, which are controlled to ensure consistency in resultant texture and SPP size for a given process.

The texture of a given component can affect certain thermal or mechanical properties (see Sections B.2 and B.3 of the LTR). The consideration of specific material properties in design basis analysis of different fuel assembly components are summarized in Table 4-1 of the LTR. One dominant effect of texture is the influence on the irradiation growth performance of the component on account of the (1 – 3F) sensitivity to the texture parameter F for the direction of interest (see Section B.4 of the LTR). An example where differences in texture are part of design is [[

]]

The SPP size and distribution affects primarily the corrosion performance of the component. The actual performance will depend on the exposed environment, including temperature, time and exposure (fluence) and water chemistry. As discussed in Part a, [[

]] GNF conducts nodular corrosion tests under [[ ]] that are based on the two-step test described by Cheng, et al. in Reference 7-1. In that work, the two-step corrosion weight gain of samples taken from the plenum section was compared with observed fuel rod corrosion, and a low weight gain from the two-step test was correlated with low in-reactor corrosion. [[

]] The same evaluation is performed for GNF-Ziron and Zircaloy-2. In some cases, [[ ]] some results for cladding are shown in Figure 2-10 of the LTR. It should be noted that [[

]] shown in Figure 15 of Reference 7-1, and that all samples in Figure 2-10 [[ ]]. The different components (Zircaloy-2 or

GNF-Ziron) had [[ ]]. The range of SPP sizes [[ ]] on the adequacy of the component’s corrosion performance.

Reference

7-1 Cheng, et al., “Development of a Sensitive and Reproducible Steam Test for Zircaloy Nodular Corrosion,” Zirconium in the Nuclear Industry, 7th Int’l Symposium, ASTM STP 939, p257-283, 1987.

RAI 8

The LTR states that an In-Process Heat Treatment (IPHT) will be offered as an added measure to prevent nodular corrosion. Has the IPHT been applied to LUAs? If so, what was the resulting performance? If this IPHT process has not been demonstrated with the proposed ZIRON cladding how can it be assured the performance will be satisfactory using this process for GNF-Ziron?

RESPONSE TO RAI 8

IPHT [[ ]]. One LUA program (at Plant F in Europe) has [[ ]]. Updated inspection results from the LUAs are provided in the response to RAI 1.

The purpose of IPHT is to provide greater corrosion margin. As corrosion is the result of cladding reacting to the exposed environment, the actual corrosion response is dependent on the exposed environment. In the context of cladding performance, corrosion margin is expected to be reflected only under adverse, off-normal conditions, such as when reactor water chemistry deviates from the targeted range. Under normal operating conditions, the improved corrosion margin is not expected to result in reduced corrosion; rather, similar degree of corrosion is expected. The corrosion margin effect can be demonstrated in the laboratory by varying appropriate test parameters, such as temperature and pressure.

[[ ]] In tests at the Halden reactor, Table 2-1 showed [[ ]]. Likewise, IPHT cladding is expected to have greater corrosion margin than non-IPHT cladding. Corrosion margin can be demonstrated in laboratory tests. Figure 2-9 shows corrosion test data after testing in steam at 400°C, which is a test condition considerably less severe than under the two-step [[ ]] shown in Figure 2-10. Note that the two-step test used is based on that developed with the correlation to in-reactor corrosion performance (Reference 8-1). In Figure 2-10, [[ ]] (Zircaloy-2). Under the less severe test condition at 400°C, Figure 2-9 shows that [[ ]].

The data shown in Figures 2-9 and 2-10 were generated from cladding [[ ]] Table 8-1 below shows the average weight gain from the two-step test (referred to as the MATAR test in Table 8-1) and the 400°C (G2) test for GNF-Ziron and Zircaloy-2 [[ ]].

Table 8-1 Average Weight Gain from the MATAR Test and the G2 Test

Material	Zircaloy-2		Ziron	
[[				

]]

The data shows that for Zircaloy-2, [[ ]] under both test conditions.

The overall conclusion is that GNF-Ziron has [[ ]] relative to Zircaloy-2.

Reference

8-1 Cheng B. *et al.*, "Development of a Sensitive and Reproducible Steam Test for Zircaloy Nodular Corrosion," Zirconium in the Nuclear Industry, 7th Int'l Symposium, ASTM STP 939, Adamson R. B. and Van Swam L. F. P., Eds., ASTM, Philadelphia, 257-283, 1987.

RAI 9

Please provide the design basis linear heat generation rate limit (limiting design in terms of rod average power) versus peak pellet exposure for designs with GNF-Ziron.

RESPONSE TO RAI 9

GNF fuel linear heat generation rate (LHGR) operating limits are specified in the form of peak LHGR as a function of [[

]]

To provide an example, the peak LHGR versus PPE limits for the UO_2 rod in GNF2 fuel design for BWR/3-6 plants are shown in Figure 9-1 below.

[[

]]

Figure 9-1 GNF2 for BWR/3-6 Plants UO_2 LHGR versus PPE Limit

Reference

9-1 Global Nuclear Fuel, "The PRIME Model for Analysis of Fuel Rod Thermal Mechanical Performance," Technical Bases - NEDC-33256P-A, Revision 1, Qualification NEDC 33257P-A, Revision 1, and Application Methodology - NEDC-33258P-A, Revision 1, September 2010.

RAI 10

What uncertainty is applied to GNF-Ziron predicted oxide thickness considering the amount of data available?

RESPONSE TO RAI 10

The only difference in chemical composition of GNF-Ziron relative to Zircaloy-2 is [[

]] under typical BWR water chemistry conditions.

For comparison, the existing GNF Zircaloy cladding oxide thickness best-estimate model and uncertainty used in PRIME thermal-mechanical (T-M) licensing analyses are plotted with Zircaloy-2 and GNF-Ziron measurements overlaid in Figure 10-1. This model is based on MELO (Maximum Effective Liftoff) data obtained from eddy-current (EC) measurements for modern GNF cladding from a variety of plants and was reviewed as part of the NRC review and approval of PRIME (Reference 10-1). The GNF-Ziron data are consistent with expectations and with the existing GNF corrosion model and uncertainty.

[[

]]

Figure 10-1 GNF Cladding Corrosion Model

GNF recognizes that the amount of available data for GNF-Ziron measurements [[

]]

Reference

10-1 Global Nuclear Fuel, "The PRIME Model for Analysis of Fuel Rod Thermal Mechanical Performance," Technical Bases - NEDC-33256P-A, Revision 1, Qualification NEDC 33257P-A, Revision 1, and Application Methodology - NEDC-33258P-A, Revision 1, September 2010.

RAI 11

The following are related to the mechanical properties of GNF-Ziron.

a. Please provide the sample geometry of mechanical test specimens discussed in Section B.3.b. Please provide additional justification for the applicability of these tests as indicators of failure strains in service applications of full size components.

b. Strain data has been provided in terms of total elongation in Figure B-5. It has been shown that total elongation is not a good estimate of ductility at failure due to its stochastic behavior. Please provide the data (tabulated and plotted) in terms of uniform elongation, identifying the test temperature, fluence, hydrogen level, and test specimen geometry.

RESPONSE TO RAI 11

a. In Figure B-3, the tests done at room temperature (RT), 288 and 343°C following irradiation in Plant K were prepared from cladding tubes with geometry indicated below (dimensions in mm). The gage length is 12.7 mm.

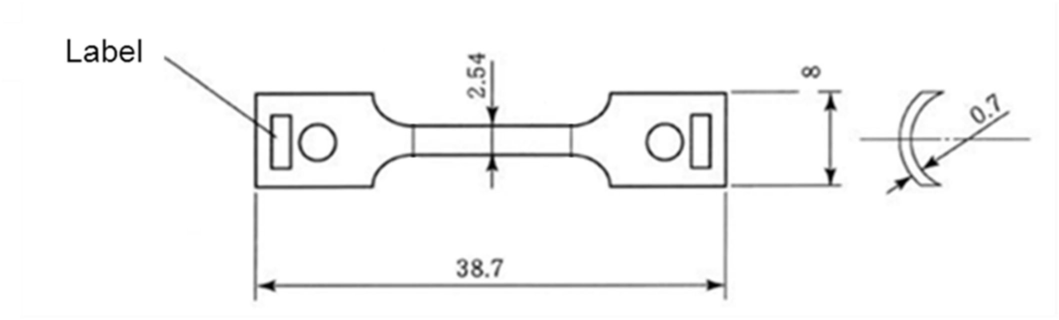

The 300°C tests in Figure B-3 were conducted using mini tensile specimens. The geometry is shown below, with all dimensions given in inches.

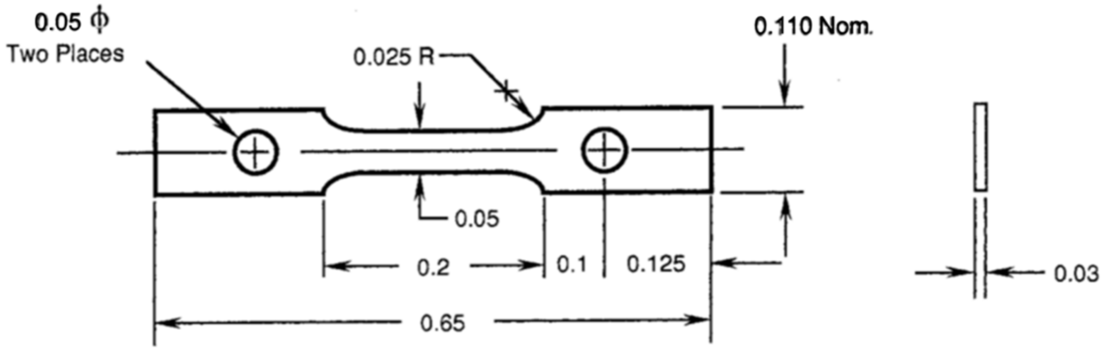

In Figure B-2, all tests were conducted on production cladding tubes. The RT tests were conducted using 12-inch long tubes, and elevated temperature tests were conducted using 30-inch long tubes. For both tests, 2-inch gage length is used for assessing strain.

Section B.3.b of the LTR has no specific discussion regarding applying the strain results as indicators of failure strains in service applications of full size components. The test data shown in Section B.3.b of the LTR are presented to show [[ ]]. The section included discussions on factors that can affect the plastic deformation behavior of Zr-alloys, such as temperature, neutron irradiation, as well as composition and material condition. The main purpose was to demonstrate [[ ]]. Tested without the influence of neutron irradiation on as-fabricated cladding tubes, the results (Figure B-2 in the LTR) show that [[ ]]. Tensile testing of irradiated cladding tubes additionally included the effect of radiation defects and hydrogen effects (from corrosion). The results shown in Figures B-3 to B-5 in the LTR were obtained from irradiated, unfueled cladding tubes that were exposed to the coolant. The yield and ultimate strengths of irradiated GNF-Ziron and Zircaloy-2 [[ ]] For actual components where the loading geometry differs from the tensile test configuration, the failure strain is expected to be different than the values shown in Section B.3.b, depending on the specific loading geometry. In the absence of significant hydrogen embrittlement, the failure strains are expected to [[ ]] as shown by the tensile test results.

b. The majority of tests, specifically those tested at room temperature, 288 and 343°C shown in Figure B-5 were reported without post-yield uniform elongation and hydrogen content. Hydrogen content was measured for two high fluence samples, one Zircaloy-2 and one GNF-Ziron, as were the associated stress-strain curves, from which post-yield uniform elongation could be extracted. These uniform strain data are shown in Table 11-1 below together with results for tests conducted at 300°C, which had reported post-yield uniform elongation but not hydrogen content. The test data used to generate Figure B-5 is shown in Table 11-1 below with associated test temperature, fluence, test specimen gage length, and, where available, uniform elongation and hydrogen level; see response to Part a of RAI 11 for specimen geometry description. Available uniform strain data is plotted in Figure 11-1 below against fast neutron fluence.

Table 11-1 Test Data Used to Generate LTR Figure B-5

Alloy	Fluence ($10^{25}m^{-2}$) (E>1MeV)	0.2% YS (MPa)	UTS (MPa)	Uniform Elongation* (%)	Total Elongation* (%)	Temp (°C)	Gage length (mm)	H (ppm)
[[								
								]]

Alloy	Fluence ($10^{25}m^{-2}$) (E>1MeV)	0.2% YS (MPa)	UTS (MPa)	Uniform Elongation* (%)	Total Elongation* (%)	Temp (°C)	Gage length (mm)	H (ppm)
[[								

]]

[[

]]

Figure 11-1 Available Uniform Strain Data

RAI 12

The following are related to GNF-Ziron irradiated creep.

a. Section B.3.f provided the results of only one creep specimen (creep measured at four levels of fluence) to characterize the GNF-Ziron creep rate at one pressure level. Are there other GNF-Ziron irradiated creep tests at other stress levels? Is the pressure level quoted in this section a hoop stress rather than an internal pressure as stated? The level is high for an internal pressure value? Please provide a comparison of the GNF-Ziron creep data to the Zr-2 creep model. What uncertainty is assumed for GNF-Ziron creep given the very small amount of irradiated creep data used to verify the GNF-Ziron creep model?

b. Has cladding creepdown been measured on the LUAs with GNF-Ziron? This should be a standard measurement? If so, please provide PRIME comparisons to these data.

RESPONSE TO RAI 12

The value quoted as a pressure level in LTR Section B.3.f is a hoop stress. This will be corrected in the –A version of the LTR. Following is the corrected sentence:

> "In the irradiation program at Plant K, creep specimens of GNF-Ziron, and Zircaloy-2 for comparison, ~~pressured~~ were pressurized to a hoop stress level of 150 MPa were assessed for creep strain after 1, 2, 4 and 6 cycles of irradiation at ~560K."

This response consists of general discussion applicable to both 12a and 12b, followed by specific discussions of 12a and 12b, respectively.

As discussed in Reference 12-1, [[

]]. Data to confirm the expectations above is presented in Reference 12-1.

a. The only irradiation creep data available for GNF-Ziron cladding under an internal overpressure is shown in Reference 12-1 Section B.3.f. The data was obtained from creep strain measurements on pressurized tubes irradiated at approximately 280°C in a commercial reactor. Creep strain data for Zircaloy-2 cladding was also included for comparison. Creep was determined after 1, 2, 4 and 6 (~14-month) cycles of operation. The average fast flux for the GNF-Ziron tube was approximately 5 x 10^{13} n/cm^2-sec; the tubes were pressurized to produce a hoop stress of approximately 150 MPa. As shown in Figure B-10 of Reference 12-1, after an adjustment is made for differences in fast flux, the creep response of Zircaloy-2 and GNF-Ziron [[

]]

A comparison of the Zircaloy-2 creep model strain predictions, using the PRIME creep model, to the GNF-Ziron measured strains is presented in Figure 12-1. As shown in Figure 12-1, the Zircaloy-2 creep model predicts [[

]]

[[

]]

Figure 12-1 Predicted (PRIME Creep Model) vs Measured Creep for GNF-Ziron

[[

]] As an example, for PRIME-based licensing analyses, the PRIME Zircaloy-2 RXA creep model, which has been recently reviewed and approved by the NRC, would be applied. Licensing application includes fuel temperature, cladding strain, and rod internal pressure analyses, along with the application of the PRIME creep model to the calculation of critical rod internal pressure indicating cladding liftoff (Reference 12-2). Cladding liftoff refers to the scenario where cladding creep(out) rate exceeds the fuel pellet swelling rate, opening the fuel and cladding gap, and is a limiting design and licensing criteria at high exposures. [[

]]

b. The creep response of cladding under rod external overpressure conditions (creepdown) affects the point in operation when closure of the as-fabricated pellet-cladding gap occurs, which in turn affects pellet-cladding mechanical interaction (PCMI) and cladding stresses and strains during subsequent operation. Creepdown response occurs at relatively low stress conditions and is determined primarily from profilometry measurements performed during post-irradiation examination (PIE) of rods after one or more cycles of operation.

   Cladding profilometry measurements have been performed on LUAs with GNF-Ziron. Profilometry measures the axial cladding outside diameter (OD) profile that includes corrosion oxide and tenacious surface crud. Therefore, comparisons of profilometry from Zircaloy-2 and GNF-Ziron fuel rods with similar environmental and operating histories would then provide a valid comparison of cladding creepdown.

   Profilometry measurements from Zircaloy-2 and GNF-Ziron fuel rod cladding from symmetric pairs of fuel rods from lead use assemblies (LUAs) irradiated in Plant H are shown in Figure 12-2. It is noted that the figures do not include uncertainty associated with the profilometry measurement system, such as calibration variation and/or reproducibility, [[ ]]. Also, the figures [[

   ]]

   GNF demonstrated that PRIME adequately predicts cladding creepdown in PRIME NRC RAI 21 (Reference 12-2). As discussed in Reference 12-1, GNF plans to apply [[

   ]] As a result, because the profilometry comparisons demonstrated that [[

   ]]

[[

]]

Figure 12-2 Profilometry Measurements from Plant H for GNF-Ziron and Zircaloy-2 Fuel

[[

]]

Summary

GNF recognizes that the amount of available data for GNF-Ziron creep measurements is small relative to Zircaloy-2. However, (1) based upon [[ ]], (2) based upon the [[ ]] and (3) based upon the [[ ]]

References

12-1 Global Nuclear Fuel, “Application of GNF-Ziron to GNF Fuel Designs,” NEDC-33353P Revision 0, December 2010.

12-2 Global Nuclear Fuel, “The PRIME Model for Analysis of Fuel Rod Thermal-Mechanical Performance Part 1-Technical Bases,” NEDC-33256P-A Revision 1, September 2010.

RAI 13

The following are related to irradiation growth.

a. Provide a detailed discussion of how the data in Figure B-11 is adjusted based on the basal F-factor in the longitudinal direction considering data with different F-factors.

b. Please provide GNF-Ziron growth data for fuel rods, tie rods (if used in current designs) and channels. Which assembly component that utilizes GNF-Ziron has the largest axial stress - tie rods, water rods or another component? Please compare axial growth for the GNF-Ziron component with greatest axial stress to the component with the least stress. Recent experience with other zirconium alloys has suggested that growth may be stress dependent even when including creep effects.

RESPONSE TO RAI 13

a. For irradiation growth of Zr-based alloys, the texture effect is generally treated by a (1-3f) term, where f is the basal pole texture factor in the direction of interest, in this case the longitudinal direction. Figure B-11 of Reference 13-1 included data from cladding and channel materials, which, because of the differences in manufacturing process, have different crystallographic texture (see Section A.3.b of Reference13-1). For the purpose of accounting for texture effect, an f value of [[ ]] is used to provide a common basis for comparison of the data plotted on Figure B-11 of Reference 13-1. To perform the normalization, the reported growth value is adjusted by [[ ]] for each of the data, where f_m is the measured f value for the corresponding data.

b. GNF-Ziron growth data for basic fuel rods (i.e., non tie rods) is provided in Figure 13-1 along with Zircaloy-2 basic fuel rods. The data points represent average fuel rod growth for a bundle. If error bars are provided, the endpoints of the error bars represent the maximum and minimum rod growth for that same bundle. If error bars are not provided, the data points represent the rod growth for that single fuel rod (i.e., all rods in the corresponding bundle were not measured). Updated water rod growth data is provided in Figure 13-2 including data that was not available at the time the GNF-Ziron LTR (Reference13-1) was prepared (originally provided in Figure B-12 of the GNF-Ziron LTR). Because channels are not offered for GNF-Ziron, no channel data is provided.

   The assembly component(s) with the largest axial stress due to bundle design mechanical loading are the tie rods, due to the tensile load imposed by the compression of the expansion springs on the basic rods within the bundle. All fuel rods are subject to additional sustained tensile axial stresses imposed by the fuel pellet column expansion during operation and due to internal overpressure within the rods. The magnitude of the axial stress imposed on the tie rods by the expansion springs on the basic rods within the bundle is [[

   ]] growth for tie rods relative to basic rods. This is demonstrated in Figure 13-3 for Zircaloy-2 fuel rods using average growth. Based on

Figure 13-3, tie rod growth is [[ ]] fuel rod growth. Water rods in the GNF fuel assembly design have low axial growth compared with fuel rods.

To compare axial growth for the bundle Ziron component with the greatest (sustained) axial stress to the component with the lowest (sustained) stress, GNF-Ziron basic fuel rod growth is compared to GNF-Ziron water rod growth in Figure 13-4. No GNF-Ziron tie rod data is currently available. To compare axial growth for the bundle component with greatest axial stress to the component with the lowest stress, Zircaloy basic fuel rod growth is compared to Zircaloy-2 water rod growth in Figure 13-5. Based on the [[

]] is anticipated.

Reference

13-1 Global Nuclear Fuel, "Application of GNF-Ziron to GNF Fuel Designs,, NEDC-33353P Revision 0, December 2010.

[[

]]

Figure 13-1 Basic Fuel Rod Growth

[[

]]

Figure 13-2 Updated Water Rod Growth of GNF-Ziron and Zircaloy-2

[[

]]

Figure 13-3 Zircaloy-2 Basic Fuel Rod Growth and Zircaloy-2 Fuel Tie Rod

[[

]]

Figure 13-4 GNF-Ziron Basic Fuel Rod Growth and GNF-Ziron Water Rod Growth

[[

]]

Figure 13-5 Zircaloy-2 Fuel Tie Rod Growth and Zircaloy-2 Water Rod Growth

RAI 14

The following are related to the impact of GNF-Ziron response to LOCA and associated analyses.

a. Have Equivalent Cladding Reacted tests been performed on high burnup GNF-Ziron cladding with hydrogen present and oxide on ID?

b. Does the addition of iron impact the α → α + β transformation temperature?

c. Please compare the rupture strains compiled from the rupture tests associated with Figure B-6 to those measured for Zr-2 [[ ]]. Also, please describe how assembly flow blockage is determined from predicted rupture strains for GNF-Ziron.

d. How does the introduction of GNF-Ziron for fuel rod design impact the Emergency Core Cooling System performance?

RESPONSE TO RAI 14

a. High temperature steam oxidation tests to different levels of equivalent cladding reacted (ECR) and associated post-quench ductility (PQD) testing have not been conducted on high burnup GNF-Ziron cladding. Currently, there is a [[ ]] Based on the data for irradiated and hydrogen pre-charged Zr-alloys in NUREG-6967 (Figures 237 and 238) (Reference 14-6), this level of hydrogen in irradiated GNF-Ziron is not expected to significantly degrade the ECR level that would still retain sufficient PQD.

b. [[ ]] on the α → α + β transformation temperature. Metallurgically, Fe, like Cr and Ni, stabilizes the beta-phase. In the Zr-rich end of binary phase diagrams, α → α + β and α + β → β transformation temperatures decrease with increasing alloying addition. In contrast, elements like Sn and O stabilizes the alpha phase. As indicated in Table A-1 of the LTR, both GNF-Ziron and Zircaloy-2 have a range in these key alloying elements, and each can have an influence on the transformation temperature. A range in the transformation temperature is therefore possible for each alloy. The [[ ]] would have a significant effect on the transformation temperature in light of the possible variation in composition for each alloy.

The α → α + β and α + β → β transformation temperatures have been examined in light of Sn, Cr and O variations within the composition range of Zircaloy-4 (Reference 14-1). In that work, O and Cr were found to affect α → α + β transformation temperature, while primarily only O affected α + β → β transformation temperature. The main effect of increasing Cr according to Reference 14-1 is to increase α → α + β transformation temperature. For Zircaloy-2, the ASTM range for Cr is between 0.05 to 0.15 wt%. Applying the results of the Reference 14-1 work to this Cr range, approximately 10°C variation can be possible for α → α + β transformation temperature. Assuming the behavior for Cr can be [[

]] in the α + β → β transformation temperature, if all other alloying elements are unchanged.

Comparative measurements of phase transformation temperatures in Zircaloy-2 to GNF-Ziron were made using differential scanning calorimetry (DSC), a technique that has been used to investigate such transformations in Zircaloys and other Zr alloys (References 14-2 and 14-3). The measurements were made at temperature ramp rates of 10 and 5°C/min. The higher ramp rate generally provided a stronger signal, while the slower ramp rate provided better resolution of the transition temperatures. In these measurements, the onset of α → α + β transformation is indicated by a sharp rise in the calorimetry signal, indicating an endothermic transformation, as the sample temperature is increased. An example comparison of results for GNF-Ziron and Zircaloy-2 at 10°C/min is shown in Figure 14-1. The comparison shows [[

]] Traces for both alloys show a sharp rise near 820°C due to two processes. The first process is the transformation to β phase occurring over a broader temperature range with a signal peak around 880 – 890°C. The second process is associated with the dissolution of second phase particles (i.e., $Zr(Fe,Cr)_2$ and $Zr_2(Fe,Ni)$) occurring over a narrower temperature range with a signal peak near 830 – 840°C. The completion temperature for α + β → β transformation (i.e., completion of transformation to β) is subject to larger uncertainties, as a sharp change is not evident in the calorimetry signal. For more consistent assessment of transition temperatures, data evaluation was carried out using software that allowed computation of various parameters including transition and peak temperatures and transformation energetics. The results at 10°C/min for GNF-Ziron showed [[

]], respectively. The results are summarized in Figure 14-2 below.

[[

]]

Figure 14-1

[[

]]

Figure 14-2

The 5°C/min results are considered more reliable due to the higher transition resolution at slower ramp rate. The results are consistent with expectations based on binary diagrams, but are not consistent with applying the trend for Cr in Zircaloy-4 (Reference14-1) to Fe.

Specific to the RAI, the DSC measurements at 5°C/min showed [[

]]
for GNF-Ziron compared to Zircaloy-2.

As the RAI is posed in connection with loss-of-coolant accident (LOCA) and associated considerations, [[
]] in relation to the onset of breakaway oxidation at or near 1000°C as discussed below. In DG-1261 (Reference14-4), the temperature for short time to breakaway oxidation is sought to the nearest 15 or 25°C. [[
]] to the test requirement. In addition, in a recent investigation (Reference14-5), it was shown that the onset of breakaway oxidation corresponded to the consumption of the oxygen-stabilized α layer, which is depleted of elements like Fe that are β-phase stabilizers, but Sn variation existed in the oxygen-stabilized α layer. Furthermore, the observed Sn variation is on a length scale that corresponded with the waviness of the oxide interface, a characteristic considered typical of breakaway oxidation (Reference14-6), suggesting that Sn variation might be responsible for the interfacial instability, perhaps through a chemical effect on the local oxidation front (Reference14-7) and hence stress build up. Considering Zircaloy-2 with GNF-Ziron in this context, [[

]] relative to Zircaloy-2.

c. In Reference14-8, Section B.3.c discussed and Figure B-6 showed that hoop stress for perforation of [[ ]] Zircaloy cladding as shown in NUREG-0630, *Cladding Swelling and Rupture Models for LOCA Analysis*, April 1980. The rupture strain for burst tests shown in Figure B-6 of the LTR can be compared with Zircaloy data. In Figure 14-3, the burst strain data for GNF-Ziron is shown with burst data for Zircaloy from NUREG-0630 only. As shown in Figure 14-3, there is considerable scatter in the burst strain for Zircaloy. When other data, such as compiled in NUREG/CR-7023, Volume 2, Revision 1, *FRAPTRAN-1.5: Integral Assessment*, October 2014, are included, there is even more scatter. However, [[
]].

[[

]]

Figure 14-3

The GEH approved LOCA evaluation methodology calculates [[ ]]. Fuel rod ballooning and perforation occur after the fuel has become uncovered, overheated and the coolant is highly voided. In GEH's approved emergency core cooling system (ECCS) evaluation methodology, [[ ]] In a BWR channel, where the flow is laterally restricted, a reduction in flow area would cause acceleration of the steam flow for the same boundary conditions. This effect would not inhibit convective heat transfer. Experimental data from National Research Universal (NRU) MT-3 tests (Reference14-9) also indicates no lack of coolability due to coplanar blockage or liftoff. Therefore, there are no coolability concerns with ballooning. As discussed above, the burst strain for GNF-Ziron [[

]] Thus the current LOCA evaluation methodology remains applicable to GNF-Ziron.

d. Primary cladding properties which affect LOCA response are corrosion behavior before the transient, strength and creep response, ductility and rupture strain and oxidation resistance during the heatup, and ductility during and subsequent to the reflood. The cladding strength and creep response affect cladding swelling and strain during the reflood. The rupture strain during heatup and cladding fracture can affect fuel dispersal during the reflood. The high temperature oxidation resistance affects the time to reach a given level of cladding oxidation or ECR. The pre-transient corrosion determines how much oxidation and hydrogen pickup occurs, which in turn can affect the post-quench ductility at a given level of ECR.

As discussed in Reference 14-8, the [[ ]]. Data confirming the expectations above is presented in Reference 14-8. Section B.3 of Reference 14-8 discusses the mechanical properties of GNF-Ziron and additional information is provided in the response to RAI 11. The creep behavior is discussed in Section B.3.f of Reference 14-8 with additional information provided in the response to RAI 12. The rupture behavior is discussed in Section B.3.c of Reference 14-8 and rupture strain is discussed further in Part c of this response. High temperature oxidation kinetics are discussed in Section B.5.a of Reference 14-8 and also in Part b of this response. Collectively, the information shows that GNF-Ziron is [[ ]], as discussed in Sections 2.3 and 2.4 of Reference 14-8. Reduced pre-transient cladding hydrogen absorption will enable a higher level of ECR during the LOCA event for acceptable post-quench ductility. Post-quench ductility of GNF-Ziron is discussed in Section B.5.b of Reference 14-8. [[ ]]

On the basis of the above, the LOCA performance of GNF-Ziron cladding is expected to [[ ]] GNF-Ziron. Any effect on the ECCS performance due to the introduction of GNF-Ziron for fuel rod design will be governed by the LOCA performance of GNF-Ziron. As the LOCA performance of GNF-

Ziron cladding is [[

]]

References

14-1 A. Miquet, D. Charquet, C. Allibert, "Effect of Cr, Sn and O contents on the solid state phase boundary temperatures of Zircaloy-4," Journal of Nuclear Materials 105 (1982) 132–141.

14-2 T. Forgeron, J.C. Barcelo, A. Castaing, J. Hivroz, J.P. Mardon, C. Bernaudat, "Experiment and Modelling of Advanced Fuel Rod Cladding Behaviour under LOCA Conditions: Alpha–Beta Phase Transformation Kinetics and EDGAR Methodology," in 12th. Int. Symposium: Zirconium in the Nuclear Industry, ASTM STP 1354, West Conshohosken.

14-3 O. Beneš, P. Van Uffelen, J. van de Laar, Cs. Gyori, R.J.M. Konings, Z. Hózer, "Kinetic studies of the α–β phase transition in the Zr1%Nb cladding for nuclear reactors," Journal of Nuclear Materials 414 (2011) 88–91.

14-4 Draft Regulatory Guide DG-1261, "Conducting Periodic Testing for Breakaway Oxidation Behavior."

14-5 Y.P. Lin, D.R. Lutz, and K. Yueh, "Factors affecting breakaway oxidation of Zr-alloys," Proceedings of the 2013 LWR Fuel Performance Meeting, Charlotte, September 15-19, 2013.

14-6 M. Billone, Y. Yan, T. Burtseva, and R. Daum, "Cladding Embrittlement During Postulated Loss-of-Coolant Accidents," US Office of Nuclear Regulatory Research, NUREG/CR-6967, 2008.

14-7 I.A. Evdokimov, V.V. Likhanskii, T.N. Aliev, V.G. Zborovskii, M.Y. Kolesnik, "On The Problem Of Theoretical Estimation Of Alloying Additives Effect On Susceptibility Of Zirconium Alloys To Nodular Corrosion," Journal of Nuclear Materials 424 (2012) 190.

14-8 Global Nuclear Fuel, "Application of GNF-Ziron to GNF Fuel Designs," NEDC-33353P Revision 0, December 2010.

14-9 "LOCA Simulation in the National Research Universal Reactor – Data Report for the Third Materials Experiment (MT-3)," NUREG/CR-2528, PNL-4166 R3, April 1983.

RAI 15

Please provide a detailed surveillance program, including PIEs, for the use of GNF-Ziron material in fuel rod and assembly design in reload applications. The PIE should include, but is not limited to, the following elements in order to verify acceptable performance: visual, oxide thickness, hydrogen level, cladding creepdown; fuel rod and water rod growth, channel growth, channel bow, and shadow corrosion.

RESPONSE TO RAI 15

GNF is committed to verifying performance of its existing and new fuel designs, including the use of GNF-Ziron through a variety of self-directed and cooperative fuel inspection programs with utilities and industry groups. Historically, GNF has performed [[ ]] fuel inspections each year as part of these activities, and intends to keep doing so. As part of this historical activity and commitment for GNF-Ziron, GNF commits to perform [[ ]] under mutually agreeable terms with a host utility. Over time, additional GNF-Ziron inspection results will become available naturally as a result of GNF's normal fuel inspection activities that are not directed explicitly at GNF-Ziron verification. Available inspection results will be provided during the technology update meeting that occurs annually between GNF and the NRC.

GNF intends to implement NSF for use in channels to mitigate channel interference, so at this time and for the foreseeable future, use of GNF-Ziron in channel applications is not anticipated. Furthermore, GNF is currently using X-750 as the spacer material in advanced fuel assembly designs, and the probability of using GNF-Ziron in spacer applications will be increasingly less common in the future. Thus, for practical considerations, near-term GNF-Ziron reloads will not include channel applications and may or may not include Ziron spacers. GNF-Ziron will be used in water rod and fuel rod applications, and therefore inspections will focus on these components. If an early reload of GNF-Ziron happens to include the older, non-X-750 spacer design in the plant that will be selected for poolside inspection, then the spacers will also be examined.

A proposed fuel inspection plan is summarized in Table 15-1. The fuel inspection will include visual inspection and length measurements of the assembled bundle and water rod. Fuel rod expansion spring compression, the tips of all fuel rods, rod-to-rod spacing, and the surface of all edge rods will be observed in this state, and will establish the gross condition of the bundle with regard to excessive corrosion or deformation. The lack of gross deformation will be indicative of normal irradiation growth and non-excessive hydrogen uptake. Typically, about eight rods in any given bundle will then be removed from the bundle and examined in detail visually and using GNF's COmbined INstrumentation System (COINS) that utilizes eddy current lift-off and profilometry measuring devices to quantify the amount of corrosion and crud buildup and assess clad creep down. Inspected rods will include a variety of pin positions that represent a variety of conditions in the bundle, including high power UO_2 edge rods away from the control blade, interior rods, full length rods, part length rods, and Gd rods. Any unusual conditions observed in an inspection will be evaluated and dispositioned.

Table 15-1 Proposed Inspection Plan for GNF-Ziron Reload Bundle

Task	Method	Comment
General condition	Bundle, fuel rod, water rod and spacer* visual	Corrosion, spalling, mechanical integrity
Cladding oxide thickness	Rod eddy current lift-off	Corrosion, includes crud
Cladding creep down	Rod diameter profilometry	Includes oxide and crud
Fuel rod and water rod growth	Visual and tape measure length	N/A
Hydrogen level	Visual and tape measure length	Gross excessive condition

*if GNF-Ziron is used in the inspected bundle rather than X-750 spacers

RAI 16

The data on shadow corrosion appears to be based on [[ ]]. This will underestimate the level of shadow corrosion due to the Inconel grids. There appears to be a small improvement compared to Zr-2 but this is based on only 2 rod comparisons such that the evidence is weak.

Please provide better measurements of shadow corrosion (such as micrographs or [[ ]]) at the spacer grids that provide a more accurate measurement of shadow corrosion.

RESPONSE TO RAI 16

Cladding shadow corrosion performance is discussed in Section 2.4.2.i of the LTR. Additional information relating to cladding shadow corrosion is provided in the responses to RAIs 1 and 4. Figures 1-4 to 1-7 and Figures 1-13 to 1-16 in the RAI 1 response include visual observations, profilometry and eddy current liftoff traces along the length of the inspected fuel rods. The majority of the figures shown is for symmetric pairs of GNF-Ziron and Zircaloy-2 fuel rods and includes visual images at spacer locations. A comprehensive set of the comparison of shadow corrosion due to the all-Inconel spacer in the GNF2 fuel assembly in GNF-Ziron and Zircaloy-2 in Plant V is shown in Figures 4-1 through 4-5 in the response to RAI 4.

Measurement of cladding shadow corrosion is presented in Figure 2-17 of the LTR. As mentioned in Section 2.4.2.i of the LTR and in the response to RAI 4, each data point for either GNF-Ziron or Zircaloy-2 (at a given axial elevation) in Figure 2-17 of the LTR represented the average [[ ]] at every elevation. [[ ]] measurements were thus represented by each data point in Figure 2-17 of the LTR. Each measurement represented the height of the liftoff peak (see Figures 1-13 to 1-16 in the RAI 1 response for example lift traces). Each measurement was the difference between the peak liftoff height at a spacer location and the liftoff just away (axially) from the spacer location. [[ ]] Figure 2-17 of the LTR.

Although Figure 2-17 of the LTR focused on the spacer locations of data gathered from eddy-current liftoff measurements, the information shown in Figure 2-17 of the LTR is very different from other eddy-current liftoff data, such as shown in Figure 2-11 of the LTR. In Figure 2-11 of the LTR, the metric plotted is the MELO or the Maximum Effective Liftoff value, which represents the [[ ]]. The MELO value is intended to show the maximum amount of corrosion (including crud deposition) away from spacer locations, and is not the suitable parameter for looking at spacer shadow corrosion effects. To assess shadow corrosion at spacer locations, the local differential at spacer locations needs to be examined, as is done and shown in Figure 2-17 of the LTR.

RAI 17

The micrograph in Figure 6.1 of the response to RAI-6 that provides hydride distribution and orientation is from an unpressurized cladding from Plant K. Plant K also had cladding that was pressurized for cladding creep.

Were micrographs taken on the pressurized cladding from Plant K or any other plant? If so did these pressurized tubes show hydride reorientation? Provide the micrographs that illustrate hydride orientation?

RESPONSE TO RAI 17

The irradiation program at Plant K included pressurized creep capsules, and the results are discussed in Section B.3.f of the submitted LTR. The tested GNF-Ziron and Zircaloy-2 capsules both had a target nominal hoop stress [[ ]]. The capsules were examined after six cycles of irradiation. A comparison of metallographic sections showing hydride distribution is illustrated below in Figure 17-1. As the capsules were sealed, only the cladding outer surface (near top of micrographs shown) experienced corrosion in both cases. GNF-Ziron picked up about [[ ]] of hydrogen, while Zircaloy-2 picked up about [[ ]] of hydrogen from the outer surface corrosion process. The morphology of the hydrides was [[ ]] hoop stress during the irradiation/corrosion period. Reorientation of the hydride is not considered to have taken place.

[[

]]

Figure 17-1 Comparison of Metallographic Sections Showing Hydride Distribution

RAI 18

The information in the LTR suggests that profilometry data were taken on GNF-Ziron and Zr-2 rods (some of these appear to be equivalent rods) from Plant V.

Please compare creepdown from the profilometry measurements from equivalent GNF-Ziron and Zr-2 rods from Plant V after one and two cycles. Also provide predictions of creepdown for these rods using the Zr-2 creep model.

RESPONSE TO RAI 18

This RAI on profilometry data and comparison with model predictions is very similar to RAI 12. Therefore, there is some overlap with the response for RAI 12.

When fuel rods are inspected using the GEH/GNF combined instrumentation measurement system (COINS), profilometry data is collected together with eddy current liftoff data. Although cladding diameter, which is of interest from the creepdown perspective, is a key contributor to the measured axial cladding OD profile, it is important to recognize that corrosion oxide and tenacious surface crud both also contribute to the measured OD profile. To ensure a valid comparison of cladding creepdown, it is therefore important to ensure that any comparisons of profilometry of Zircaloy-2 and GNF-Ziron fuel rods are between those that have experienced similar environmental and operating histories.

This RAI requests a comparison of creepdown from profilometry data from the LUA program at Plant V. Side-by-side GNF-Ziron vs. Zircaloy-2 comparisons of profilometry (and other inspection data) from the LUA program from Plant V after two cycles of operations are provided in Figures 1-13 through 1-15 in the RAI 1 response. However, as noted in the response to RAI 1, the inspected LUA [[

]]

The response to RAI 1 included profilometry measurements from Zircaloy-2 and GNF-Ziron fuel rod cladding from symmetric pairs of fuel rods from the LUA irradiated in Plant H. This is also discussed in more detail in the response to RAI 12. As discussed in response to RAI 12, the profilometry data in essence [[

]]

With respect to the prediction of cladding creepdown, GNF demonstrated that PRIME adequately predicts cladding creepdown in PRIME USNRC RAI 21 (Reference 18-1). GNF plans to [[

]]

Reference

18-1 Global Nuclear Fuel, "The PRIME Model for Analysis of Fuel Rod Thermal-Mechanical Performance Part 1-Technical Bases," NEDC-33256P-A, Revision 1, September 2010.

RAI 19

In the LTR supporting the irradiation of LUAs in Hatch 2 (GNF-0000-0079-7396NP, DRF Section 0000-0079-7396 R6, January 2013), there is a comparison of the ASTM Zr-2 (UNS R60802) specification composition, with GNF's proprietary Controlled Chemistry (CC) Zr2 and GNF-Ziron. It is understood that GNF's CC Zr-2 contains a tighter range on the alloying elements, [[ ]], and this would be representative of GNF's experience. Various references (1- 8) refer to a High Fe/Zry-2 or High-Fe Improved Zircaloy by 2000, and ultimately GNF-Ziron by 2006. The most common nominal composition (in wt%) was given as 1.46 Sn, 0.26 Fe, 0.10 Cr, and 0.05 Ni, with balance Zr, although Lutz and Lin (Reference 1) report a High Fe Zr-2 with 1.5 Sn, 0.25 Fe, 0.10 Cr, and 0.05 Ni.

The LTR provides the range of Fe content as [[ ]]. The ranges of Sn, Cr, Ni, and O are also provided, however the nominal values of Sn, Ni, and O in GNF-Ziron are not provided, although it is expected that they would probably be near the mid-range values, e.g., [[ ]], which is cited in the LTR.

The O content does have an influence on phase transformation (α → α + β and α + β → β) as well as strength. In LTR section B.3.b, Tensile Properties, GNF states that the apparent [[ ]] than normally used in GNF's Zr-2.

a. What is the nominal value for Sn and O in GNF-Ziron? What are the anticipated ranges during manufacturing?

b. Are there any tests of irradiated GNF-Ziron with Fe at the upper limit [[ ]], or higher?

c. Please indicate the nominal composition and heat treatment (e.g., IPHT) of the GNF-Ziron alloy irradiated in each program, this will provide information on the alloy range tested.

REFERENCES

1. D. R. Lutz, C. C. Lin, "BWR Zircaloy Corrosion and Water Chemistry Tests," TR-106830, EPRI, December 1996.
2. Etoh, Y., Shimada, S., Yasuda, T., Ikeda, T., Adamson, R. B., Chen, J.-S. F., Ishii, Y., and Takei, K., "Development of New Zirconium Alloys for a BWR," Zirconium in the Nuclear Industry: Eleventh International Symposium, ASTM STP 1295, E. R. Bradley and G. P. Sabol, Eds., American Society for Testing and Materials, 1996, pp. 825-849.
3. Shinji Ishimoto, Toshio Kubo, Ronald B. Adamson, Yoshinori Etoh, Kunio Ito, Youjiro Suzawa, "Development of New Zirconium Alloys for Ultra-High Burnup Fuel," Proceedings of the ANS International Topical Meeting on LWR Fuel Performance, Park City, 2000, pp. 31-42.
4. K. Une and S. Ishimoto, "Heat Capacity of hydrogenated Zircaloy-2 and high Fe Zircaloy-2," Journal of Nuclear Materials 323 (2003) 101-107.

5. K. Une and S. Ishimoto, "Dissolution and precipitation behavior of hydrides in Zircaloy-2 and high Fe Zircaloy," Journal of Nuclear Materials 322 (2003) 66-72.
6. Shinji Ishimoto et al., "Improved Zr Alloys for High Burnup BWR Fuel, "Proceedings of Top Fuel 2006, Salamanca, Spain (2006).
7. Hideo Soneda, Yutaka Iwata, Mitsuo Ebisuya, et al, "BWR Core and Fuel Development for Highly-economical Power Generation," Hitachi-GE Nuclear Ltd, 2009 (Hitachi-r2009_02_104.pdf).
8. K. Une, K. Sakamoto, M. Aomi, J. Matsunaga, Y. Etoh, I. Takagi, S. Miyamura, T. Kobayashi, K. Ito, "Hydrogen Absorption Mechanism of Zirconium Alloys Based on Characterization of Oxide Layer," Journal of ASTM International (JAI102950), Vol. 8, No. 5, 2011.

RESPONSE TO RAI 19

a. The composition range for GNF-Ziron is provided in Table A-1 of the submitted LTR. The Sn and O composition for GNF-Ziron is [[ ]].
For both alloys, there are no specified nominal values for alloying elements, as allowable ranges are specified. Based on experience with Zircaloy-2 in recent years, the Sn value (from ingot certificates) is centered [[ ]]

b. GNF has [[ ]] The composition of GNF-Ziron that has been used in irradiation programs is given in Part c of this response. The highest Fe content in ingot certificates is [[ ]].

c. The composition range for GNF-Ziron is provided in Table A-1 of the submitted LTR. The composition range for the ingots used in different irradiation programs is given in Table 19-1 below. As discussed in the LTR, [[ ]] In Table 19-1 below, it can be seen that the Fe content in six ingots of materials used in irradiation programs spanned [[ ]]. It is expected that the range would be broader as more ingots are produced. Consistent with Table A-1 of the LTR, GNF [[ ]] for production use.

Table 19-1 Ingot Composition Range

Plant	**Design**	**Cladding Type**	**Composition Range (from Ingot Certificates) in wt%**				
			Fe	**Sn**	**Cr**	**Ni**	**O**
K	[[						
G							
V							
H							
H							
F							
P, N							]]

<u>RAI 20</u>

In Table 2 of the LTR supporting the irradiation of LUAs in Hatch 2 (GNF-0000-0079-7396NP, DRF Section 0000-0079-7396 R6, January 2013), GNF identifies “number of properties or characteristics for GNF-Ziron were obtained through testing.” Are there any additional properties or characteristics that have been obtained through testing or measurement not provided in the LTR.

<u>RESPONSE TO RAI 20</u>

The document GNF-0000-0079-7396 was originally written in 2008 in support of the LUAs at Hatch 2 for Cycles 21, 22, and 23, before the LTR was submitted. The 2008 report was revised in 2013 to support operation of the LUA in other cycles instead of Hatch 2 Cycle 23. The 2013 revision of GNF-0000-0079-7396 did not include updating information that had become available since 2008 which was included in the submitted LTR. The submitted LTR included up-to-date information that was available at the time. Since the submittal of the LTR, some new information has been obtained; please see the responses to RAIs 1 and 4 on inspection related information, and the response to RAI 14b on information related to the $\alpha \rightarrow \alpha + \beta$ transformation temperature.

RAI 21

The performance of a fuel rod is highly dependent on its integral power. Please provide the exposure/burnup and effective full power days (EFPDs) at the end of each cycle, or the cumulative burnups and EFPDs at discharge for the various LUA programs (Plants G, P, N, V, F, and H).

RESPONSE TO RAI 21

As this RAI is related to fuel rods, only LUA programs at Plants G, V, F and H are addressed in this response, because programs at Plants P and N are related to channels, and application to the channel will no longer be within the scope of the LTR (See the response to RAI 2). For the LUA programs at Plants G, V, F and H, the cumulative burnup and operational days are summarized in Table 21-1 below. Note that in a couple of programs, the LUAs are currently in the third two-year cycle of operation. In these two cases, the burnup and operational days at the end of the second operational cycle are given.

Table 21-1 Cumulative Burnup and Operational Days

Plant	Design	Status (May 2015)	Cumulative Burnup (GWd/MTU)	Cumulative Operational Days
G	[[			
V				
H				
H				
F				

]]

RAI 22

In the LTR for GNF-Ziron (Figure B-1), GNF provided limited data on the thermal conductivity of Zr-2 and GNF-Ziron. The NRC staff agrees that the data show that the thermal conductivity measurements show that GNF-Ziron and Zr-2 have essentially the same conductivity, and given the small increase in Fe content, PNNL would expect the thermal conductivities to be essentially equal. PNNL compared the measured data with the correlation for Zr-2 provided in the GNF LTR, "The PRIME Model for Analysis of Fuel Rod Thermal – Mechanical Performance," NEDC-33256P that demonstrates the data is lower than the correlation. In addition, the data were compared with the IAEA correlation (from IAEA TECDOC 1496 (Ref. 9) and MATPRO Ref. 10). The PRIME correlation agrees well with the IAEA and MATRPRO correlations, although the IAEA correlation is slightly lower over the temperature range from 500 to 1000 K.

Please comment on the measured data for Zr-2 and GNF-Ziron thermal conductivity and the difference with the correlations used in PRIME and MATPRO, and the IAEA recommended correlation.

REFERENCES

9. IAEA-TECDOC-1496, "Thermophysical properties database of materials for light water reactors and heavy water reactors," Final report of a coordinated research project 1999-2005, IAEA, Vienna, June 2006.
10. SCDAP/RELAP5-3D© Code Manual, "Volume 4: MATPRO - A Library of Materials Properties for Light-Water-Reactor Accident Analysis," INEEL/EXT-02-00589, Volume 4, Revision 2.2, October 2003.

RESPONSE TO RAI 22

The PRIME correlation was derived from a large database of thermal conductivity measurements for Zircaloy, and as noted in RAI 22, agrees well with the MATPRO and IAEA correlations. [[ ]] Comparing the data in the LTR with the data in Figure 1 of Section 6.2.1.4 (IAEA-TECDOC-1496) it is noted that the LTR data is [[ ]] Similarly, from Figure 2 of Section 6.2.1.4 (IAEA-TECDOC-1496) it is noted that the [[ ]].

Additionally, it is noted that the PRIME application methodology includes a model uncertainty [[ ]], including cladding thermal conductivity.

In summary, it is concluded that [[

]] in the PRIME statistical application methodology.